PAPER

High-performance supercapacitors based on amorphous carbon derived from natural *Ramulus mori*†

Yaping Xu,‡[a] Renfeng Tan,‡[a] Jinggao Wu[b] and Jing Huang ✦*[a]

Using biomass waste as a supercapacitor material has been one of the most widely used methods owing to its high performance, low cost and sustainable green economy. Herein, we employ *Ramulus mori*, a silkworm industry waste, by low-cost pyrolysis and chemical activation methods to produce high-efficiency, high-power and high-energy supercapacitors. The as-prepared architectures with a large number of hierarchical pores and high specific surface areas exhibit a high specific capacitance of $\sim$796 F g^{-1} at 1 A g^{-1}, and the retention rate can reach 93.6% even after 10 000 cycles at 10 A g^{-1}. The assembled symmetrical device has a high energy density of $\sim$59 W h kg^{-1} at 1.2 kW kg^{-1}, which paves the way for the development of green electrode materials with promising applications.

1. Introduction

Owing to the inevitable depletion of non-renewable energy and the increasingly serious global environmental pollution problem, developing efficient energy storage and conversion systems is urgently needed to fulfill the demand for renewable energy and clean energy sources.[1–3] Among the energy storage devices, supercapacitors (SCs) are one of the most extensively applied devices owing to their superior power density, rapid charge/discharge potency, longer operating time, environmental sustainability and safety features.[4–6] SCs have been widely used in new energy vehicles, smart grids, urban transportation and other fields. However, the wide application of SCs is still limited due to their relatively low energy density.[7,8]

The key to the performance of supercapacitors lies in electrode materials, including carbonaceous materials, transition-metal based materials (*e.g.*, oxides, nitrides and sulfides) and conducting polymers.[9–12] Carbon materials usually have a high specific surface area, good conductivity and chemical stability, abundant reserve, and are easy to produce and process, and non-toxic.[13–16] There are currently many issues associated with

the combustion of fossil fuels and waste generation, and sustainable industrial growth is much focused on.[17] Biomass is a readily available, inexpensive, easy to modify, environmentally friendly, and renewable resource.[18–20] Usually, chemical activation with alkali hydroxides such as KOH, NaOH and LiOH or acidic compounds such as H_3PO_4 and $ZnCl_2$ is an effective method to fabricate porous activated carbon materials.[21,22] These advantages, together with the high carbon content of biomass, make it an attractive raw material for the preparation of advanced functional carbon materials in the field of supercapacitors.[23–26]

Mulberry is an environmentally friendly, widespread, and versatile plant. At present, mulberry biomass has been used for extracting active ingredients for medical research such as rutin, quercetin, 1-deoxynojirimycin, *N*-methyl-1-deoxynojirimycin, 1,4-dideoxy-1,4-imino-D-arabinitol, β-sitosterol, stigmasterol, β-sitolsterolβ-D-glucoside and γ-aminobutyric acid with high antibacterial, anticoagulation, hypotensive, hypolipemic, hyperglycemic, antitumor, antisenescence, antifilarial, and antiulcerative activities.[27–29] Large quantities of mulberry-based by-products of extraction residues are generated during the process, which could be envisaged for value-added secondary-utilization as green energy storage materials.[30,31] The total production of *Ramulus mori* in 2018 in China is in the scope of 2.844–3.555 million tons.[32] A large share of *Ramulus mori* is consumed by agro-industries where the disposal of waste *Ramulus mori* is a great issue. In this work, we report a novel bio-inspired hierarchical nanoporous carbon employing the mulberry-based by product (*Ramulus mori*) as a raw material by a facile two-step method involving carbonization and activation annealing (Scheme 1). The performance of the electrode and the supercapacitor based on *Ramulus mori* derived carbonaceous materials and the structure–activity relationship have been investigated in detail.

[a] *State Key Laboratory of Silkworm Genome Biology, Key Laboratory Of Sericultural Biology and Genetic Breeding, Ministry of Agriculture and Rural Affairs, College of Sericulture, Textile and Biomass Sciences, Southwest University, Chongqing 400715, P. R. China. E-mail: hj41012@163.com*

[b] *Key Laboratory of Rare Earth Optoelectronic Materials & Devices, College of Chemistry and Materials Engineering, Huaihua University, Huaihua 418000, P. R. China*

‡ These authors contributed equally to this work.
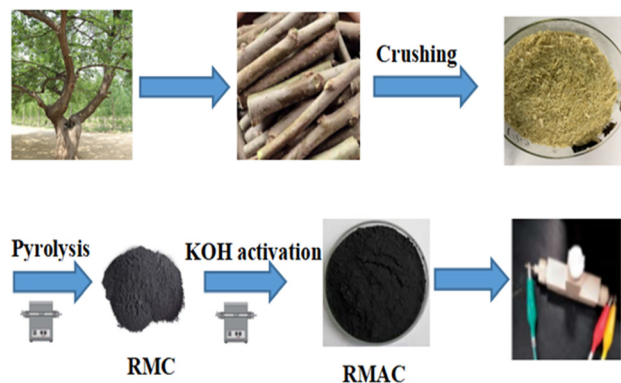
Scheme 1 Schematic illustration of the synthesis strategy of the RMAC composites.

2. Experimental section

2.1 Materials and methods

2.1.1 Materials and reagent. *Ramulus mori* was collected from the mulberry field in Southwest University Chongqing, China. *Ramulus mori* was removed from the mulberry leaf and then cut into centimeter-scale blocks and dried completely and ground into powder. Nafion solution, poly(tetrafluoroethylene) (PTFE) and acetylene black were purchased from Sigma-Aldrich. Potassium hydroxide (KOH) and all other reagents were obtained from Adamas-beta®. All chemicals were used without further purification.

2.1.2 Preparation of *Ramulus mori*-derived activated carbon (RMAC). Activated carbon was prepared by pyrolysis using *Ramulus mori* powder and KOH as raw materials. Firs, the *Ramulus mori* powder was heated in a tubular furnace under an argon atmosphere to 200 °C at a heating rate of 3 °C min^{-1}, and held at this temperature for 1 hour. Then, it was further heated to 500 °C and cooled down to room temperature after 2 hours of heat preservation. The obtained carbon was named RMC. Second, RMC and KOH with a mass ratio of 1 : 1.5 were thoroughly ground in an agate mortar. After grinding, the mixture was further heated to 700 °C according to the pyrolysis process similar to RMC in the tube furnace. Finally, the obtained carbon was named RMAC-4. For comparison, the different mass ratios of RMC and KOH (2 : 1, 3 : 2, 1 : 1, and 1 : 2) were also investigated by the above process. The samples were denoted as RMAC-1, RMAC-2, RMAC-3 and RMAC-5. In addition, RMAC-6, RMAC-7 and RMAC-8 were prepared at 600, 800 and 900 °C in accordance with the procedure similar to RMAC-4. In the whole process, all carbonized samples were neutralized with dilute HCl and washed with deionized water, and then dried at 80 °C for 12 h.

2.2 Characterization

The XRD patterns were characterized using powder X-ray diffraction (Shimadzu XRD7000). The surface morphology and structure of samples were obtained through scanning electron microscopy (FESEM, JSM-7800F) and transmission electron microscopy (TEM, JEOL 2100). Nitrogen sorption isotherms were recorded by means of an Autosorb-1 (Quantachrome Instruments). The specific surface area was reckoned through the Brunauer–Emmett–Teller (BET) method. The distributions of the pore size and the pore volume were confirmed from the adsorption branch isotherms through the density functional theory (DFT) method. And then, the total pore volume (V_t) was reckoned based on the amount adsorbed at a relative pressure P/P_0 of 0.990. The volume (V_{mic}) and surface area (S_{mic}) of the micropore were analysed on the basis of the t-plot theory. Raman spectra were obtained with a Jobin–Yvon HR 800 spectrometer. X-Ray photoelectron spectroscopy (XPS) measurements were carried out on a Thermo Fisher Scientific (Escalab 250xi, USA). Fourier transform infrared (FT-IR) spectra were acquired using a Thermo Scientific Nicolet iS 50 spectrometer.

2.3 Electrochemical measurements

For the two-electrode system, a homogeneous slurry of the electroactive material, polytetrafluoroethylene (PTFE), and acetylene black with a weight ratio of 80 : 10 : 10 in ethanol was formed and pasted to the nickel foam current collector (1 cm × 1 cm), then vacuum dried at 80 °C for 12 h. The loading of the active material for each working electrode was measured to be ~3 mg cm^{-2}. And then, a glass-fiber filter paper (Waterman, GF/B) as a separator and 1 M KOH aqueous solution as the electrolyte were used to assemble a test cell. For the three-electrode system, the working electrode was prepared through the dispersion of active carbon in mixed solution of Nafion and ethanol (1 : 20) dripping on the glassy carbon electrode. Platinum foil and Hg/HgO were used as the counter and reference electrodes, respectively. Electrochemical characterization was carried out on an electrochemical workstation (Shanghai Chenhua Instrument Co. Ltd, China).

For the two-electrode system, the gravimetric specific capacitance of a single electrode is calculated by the following equation:

$$C_{sp} = 2I \times \Delta t/m \times \Delta V \qquad (1)$$

where C_{sp} (F g^{-1}) is the specific capacitance based on the mass of the active carbons, I is the discharge current (A), Δt is the discharge time (s), ΔV is the voltage difference (except the Ohm drop) within Δt (V), and m is the loading of the active material in each working electrode (g).

For the three-electrode system, the gravimetric specific capacitance can be calculated by the following equation:

$$C_{sp} = I \times \Delta t/m \times \Delta V \qquad (2)$$

where I is the discharge current (A), Δt is the discharge time (s), ΔV is the voltage (V), and m is the mass of the active materials (g).

The energy density E (W h kg^{-1}) and the power density P (W kg^{-1}) are calculated by the following equations:

$$E = C_{sp}V^2/(2 \times 3.6) \qquad (3)$$

$$P = 3600\,E/\Delta t \qquad (4)$$

where t is the discharge time (s).

Table 1 Summary of BET characteristics of activated carbons

Sample	$S_{BET}{}^a$	$V_{tot}{}^b$	$S_{mi}{}^c$	$S_{me}{}^d$	$S_{ma}{}^e$	$V_{mi}{}^f$	$V_{me}{}^g$	$V_{ma}{}^h$
RMC	7.191	0.017	1.352	4.87	0.969	0.002	0.012	0.003
RMAC-1	423.15	0.236	103.32	205.12	114.71	0.082	0.103	0.051
RMAC-2	721.36	0.307	116.23	462.18	142.95	0.102	0.175	0.03
RMAC-3	525.34	0.315	103.25	364.57	57.52	0.086	0.201	0.028
RMAC-4	645.711	0.332	116.45	473.16	56.101	0.092	0.216	0.024
RMAC-5	756.23	0.248	136.24	503.17	117.301	0.012	0.185	0.051
RMAC-6	415.62	0.284	86.42	301.68	27.52	0.015	0.204	0.065
RMAC-7	531.84	0.139	103.42	352.46	75.96	0.01	0.082	0.047
RMAC-8	483.42	0.267	136.24	308.42	38.76	0.028	0.166	0.073

^{a} S_{BET}: BET surface area. ^{b} V_{tot}: total volume. ^{c} S_{mi}: micropore surface area. ^{d} S_{me}: mesopore surface area. ^{e} S_{ma}: macropore surface area. ^{f} V_{mi}: micropore volume. ^{g} V_{me}: mesopore volume. ^{h} V_{ma}: macropore volume.

distribution at the nanometer scale. An ordered regular pore frame construction is evident for ion diffusion/transport, and high porosity can contribute to electrolyte penetration and offer more electrochemically active sites.[49] The hierarchical structure can reduce the diffusion resistance, and improve the mass transport in the electrolyte, as well as expose more active sites, which is conducive to the enhancement of the electrochemical performance.[50] At the same time, the activation temperature also affects textural properties, such as (a BET surface area of 645.71 vs. 483.42 m^2 g^{-1}; a pore volume of 0.33 vs. 0.267 cm^{-3} g^{-1}; an average pore size of 3.186 vs. 2.183 nm; RMAC-6 vs. RMAC-8, 600 vs. 900 °C). With the increase of the activation temperature from 600 °C to 700 °C, the structure parameters indicate the same tendency. However, increasing the activation temperature to 900 °C would contribute to the collapse of the pores, and further unfavourably results in the decrease of the textural properties.

The atomic valence states and elemental composition of the composite are measured by XPS, as shown in Fig. 3. Nitrogen, oxygen, phosphorus and sulfur elements are introduced into the carbon skeleton via the pyrolysis strategy. C1s spectra (Fig. 3b) of RMAC-4 after deconvolution indicates a peak at 285.3 eV attributed to sp^3 carbon in the C–S bond.[51] The N1s core level spectra (Fig. 3c) of RMAC-4 are deconvoluted into three components as quaternary-N (NQ, 402.2 eV), amide/amines or nitrile N (NC, 399.4 eV) and oxidized-N (NX, 406.5 eV).[52] The existence of N–O in the carbon graphitic plane effectively reduces the electronic transfer resistance of RMAC-4. O1s (Fig. 3d) spectra appear in the form of P=O (531.9 eV) and P–O–P/P–O–C (533.2 eV), respectively. The hydrophilicity of the O-containing groups in RMAC-4 could be conducive to the wettability of the electrolyte interface, which results in the enhancement of the electrochemical performance.[53] The P2p spectra shown in Fig. 3e display that three peaks for 2p$_{3/2}$ at 131.4 eV, 134.4 eV, and 138 eV, which could be assigned to C–P species, pyrophosphate/polyphosphate (PP) and monophosphate/metaphosphate (MP) groups, respectively.[54] The S2p XPS spectrum (Fig. 1f) is deconvoluted to three peaks at 161.8 eV, 164.2 eV and 167.6 eV for S2p$_{3/2}$ (S1, C=S) and S2p$_{1/2}$ (S2, C–S) as well as oxidized sulfur species, which confirm the doping of the RMAC-4 network by sulphur46.[46,55]
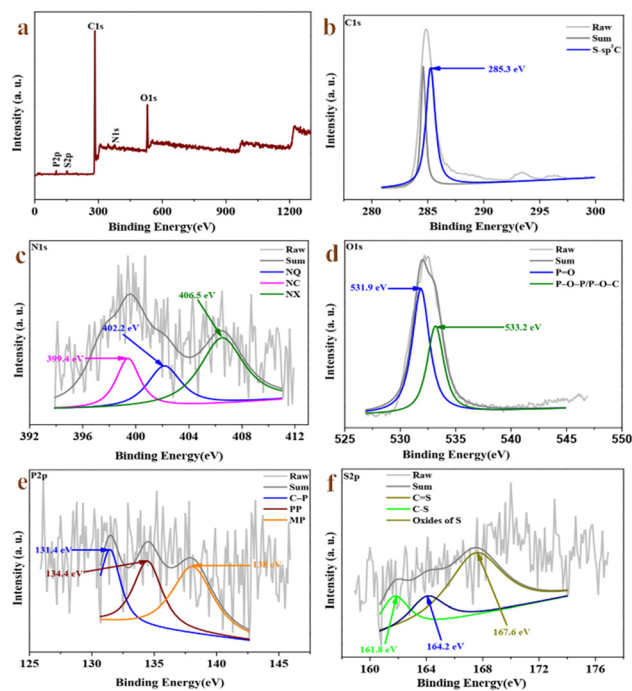
Fig. 3 (a) XPS survey spectrum of RMAC-4, (b) high resolution C1s of RMAC-4;,(c) high resolution N1s of RMAC-4, (d) high resolution O1s of RMAC-4, (e) high resolution P2p of RMAC-4, and (f) high resolution S2p of RMAC-4.

Synergistic effect originating from the multiple doping of N, O, P and S are conducive to the electrochemical reactions. On account of RMC, the presence of C, N, O, P, and S has also been confirmed by the XPS spectrum (Fig. S4a, ESI†). The C1s spectrum (Fig. S4b, ESI†) is deconvoluted into three peaks representing C=C (284.24 eV), S-sp^{3}C (284.85 eV), C–O (285.77 eV) and C=O (287.53 eV) groups.[50] The N 1s spectrum (Fig. S4c, ESI†) indicates that there are four forms of N, namely, N-6 (397.5 eV), N–C (398.3 eV), N-5 (399.3 eV) and N–Q (402.1 eV).[51] The O1s spectrum (Fig. S4d, ESI†) is fitted by two peaks, located at 532.2 and 532.8 eV, which could belong to P=O and P–O–P/P–O–C groups.[52] By fitting the P2p spectra (Fig. S4e, ESI†), three main peaks located at 131.3 eV, 133.8 eV and 135.1 eV are clearly identified, which indicate the existence of C–P species, pyrophosphate/polyphosphate (PP) and monophosphate/metaphosphate (MP) bonds.[53] The S2p (Fig. S4f, ESI†) peaks centered at 164.4, 168 and 172 eV C–S/C=S correspond to C=S, C–S and oxides of sulfur, respectively.[54] Based on the XPS results, the surface chemistry of RMAC-4 and RMC has been altered owing to the activation of KOH, consistent with the FTIR spectra.

3.2 Electrochemical behaviors of the electrode

The CV curves of RMAC samples at 100 mV s^{-1} are shown in Fig. 4a and Fig. S5 (ESI†). All electrodes display a similar rectangular shape and a small redox peak, confirming that a typical electrical double layer capacitance (EDLC) reaction occurred on the surface of these electrodes in 1 M KOH, which is ascribed to the rapid spreading of ions along with the low
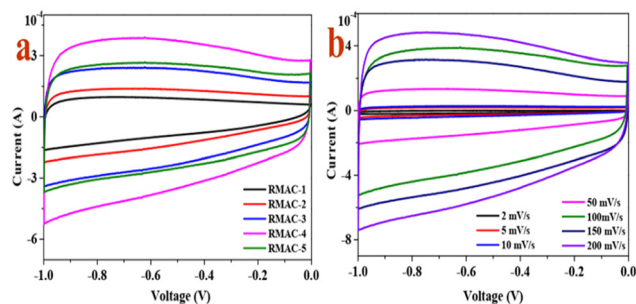
Fig. 4 (a) CV curves of RMAC samples prepared under different ratios of precursor/KOH at 100 mV s^{-1} and (b) CV curves of RMAC-4 at different scan rates.

Fig. 5 (a) Nyquist plots of RMAC-4 and (b) galvanostatic charge/discharge curves of RMAC-4 at different current densities.

diffusion resistance within the hierarchical pore structure.[56] Meanwhile, all the samples have indicated a pair of reversible humps, which confirm capacitive action deriving from the electrical double layer formation and the faradaic redox reactions related to the doping with heteroatoms such as N/O/P/S-containing functional groups.[57] On account of the CV area, the largest CV area for the RMAC-4 electrode has confirmed the highest capacitance, which can be ascribed to ultrafast ion transfer derived from the specific surface area and hierarchical porous configuration.[58] The CV curves of the RMAC-4 (Fig. 4b) composite at different scan rates ranging from 2 to 200 mV s^{-1}, which exhibits an almost rectangular "mirror-like" rectangular-shaped CV curve. Moreover, the CV rectangular curves of RMAC-4 have also been obtained even when the scan rate is as high as 200 mV s^{-1}. The hierarchical pore structure ensures an ultrafast electrochemical reaction between RMAC-4 and the electrode. The very low electrochemical reaction rate is attributed to the electrolyte ions which diffuse into the interior of the pores by passing a very long distance.[59] The hierarchical pore structure of the RMAC-4 electrode instead could be conducive to shorten diffusion paths. In addition, the electronic conductivity of the entire electrode is further improved by the activation of KOH, which is highly conductive after electrochemical doping.[60]

The EIS tests are carried out to estimate the resistance and capacitive performances of materials in view of the kinetics information correlated to the electron/ion transport procedure and the electrochemical performance. As for the Nyquist plots (Fig. 5a), a steep line is in the low-frequency range and a semicircle is at medium frequencies, as well as intercepted with the real axis in the high-frequency region.[61] The intercept of the plot and *x*-axis is assigned to the internal resistance (R_s), which is correlated to ohmic contact, including the intrinsic resistance of the active material, ionic resistance of the electrolyte and contact resistance of the current collector. Clearly, the R_s of RMAC-4 (1.56 Ω) at 106 kHz is small, which confirms the low charge transfer resistance. Additionally, the diameter of the semicircle refers to the interface charge transfer resistance (R_{ct}), confirming the electron transfer derived from the electrolyte to the RMAC-4. RMAC-4 indicates a lower R_{ct} value, which implies its higher electrical conductivity and its electron
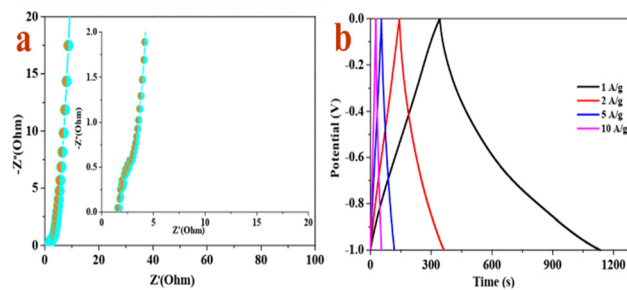
transfer dynamics. The straight line with a steeper slope in the low frequency region also manifests a superior diffusion performance of RMAC-4, which is attributed to the hollow tube and slice structure. The special configuration of RMAC-4 could refrain from the "dead volume" and further contribute to the increase of the specific surface area and a shorter channel for the diffusion of electrolyte.[62] Hence, the electrochemical results suggest that the RMAC-4 matrix could contribute to the enhancement of the electronic conductivity of the electrode and improved ion diffusivity, as well as overall electrolyte wettability.

Fig. 5b verifies the rate capability of the RMAC-4 electrode by measuring GCD at different current densities ranging from 1 to 20 A g^{-1}. According to the curves, an isosceles triangle shape with slight distortion and no obvious IR drop even at 20 A g^{-1} could be observed. Fig. 5b illustrates that the charge–discharge time decreases with the enhancement of the current density. The measured specific capacitance values at the current densities of 1–20 A g^{-1} are 795.94, 446.72, 289.43, 208.35, 182.34 F g^{-1}, respectively. The lowered capacitance at higher current densities such as 182.34 F g^{-1} at 20 A g^{-1} could be attributed to the short diffusion duration at the active site of the electrode surface with a rapid rate under a high current according to the migration of K$^+$/H$^+$ ions in the electrolyte. Moreover, RMAC-4 with a low specific surface (645.711 m^2 g^{-1}) still could indicate superior electrochemical performance, which is ascribed to the rational distribution of nanopores and improved surface wetting ability of the electrolyte due to the doping of heteroatoms from the component of *Ramulus mori*.

In order to optimize the electrochemical characteristics of the electrode, RMAC composites are synthesized at different pyrolysis reaction temperatures and different ratios. According to the effect of the ratio (RMC/KOH) on the properties (Fig. 6a), the specific capacitance of RMAC-4 obviously exceeds those of other RMAC samples (1:1.5 *vs.* 2:1 *vs.* 3:2 *vs.* 1:1 *vs.* 1:2; ~796 *vs.* ~190 *vs.* ~433 *vs.* ~325 *vs.* ~392 F g^{-1} at 1 A g^{-1}; RMAC-4 *vs.* RMAC-1 *vs.* RMAC-2 *vs.* RMAC-3 *vs.* RMAC-5). The superior performance of RMAC-4 is ascribed to the broader continuous 3D porous frame structure, which could be beneficial for the infiltration of the electrolyte and transport of ions as well as current collection.[63] Notably, RMAC-4 delivers a higher capacity of ~796 F g^{-1} compared with RMC
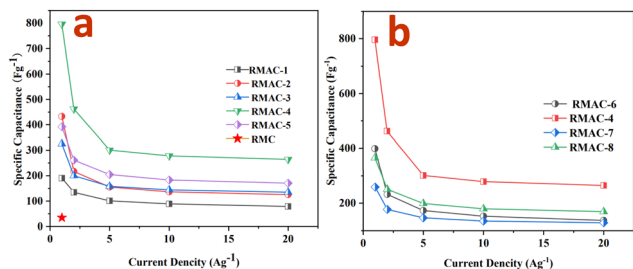
Fig. 6 (a) Capacitances of RMAC samples prepared under different ratios of precursor/KOH at different current densities and (b) capacitances of RMAC samples prepared under different temperatures at different current densities.

($\sim$34 F g^{-1}) at 1 A g^{-1}, which is also more superior than other carbon materials derived from biomass such as cellulose, bagasse, pomelo peel, and so on.[64] Fig. 6b shows the variation of specific capacitance with respect to temperature. The results of the prepared RMAC composites demonstrate that the values of specific capacitance at temperatures of 600, 700, 800, and 900 °C are $\sim$399, $\sim$796, $\sim$259 and $\sim$365 F g^{-1} at 1 A g^{-1}, respectively. Additionally, the specific capacitance values of the electrodes decrease to $\sim$79, $\sim$125, $\sim$135, $\sim$265, $\sim$171, $\sim$137, $\sim$128 and $\sim$169 F g^{-1} for RMAC-1 to 8, respectively, at a current density of 20 A g^{-1}. The electrodes retain 41.31, 28.95, 41.59, 33.25, 43.52, 34.28, 49.45 and 46.18% of their charge storage capacity with the increase of the current density from 1 to 20 A g^{-1}. The superior performances are attributed to the good rate capability, which could be applied in fast-charging devices. The whole tendency demonstrates that the specific capacitance decreases with the increase of current density, by virtue of restrictions of the diffusion movements of electrolyte ions. The internal active sites of RMAC electrodes at low current densities could be fully utilized by virtue of low ohmic drop, which could provide sufficient time for redox reactions and further lead to the high specific capacity.[65] Whereas, the low capacities at high current densities are attributed to inevitable time constraint by virtue of the high charge–discharge rate. Therefore, the mobility of ions in the electrolyte rely on diffusion, and the charge storage center is subject to the outer surface.[66] In a word, the results evidence that the optimized RMAC-4 electrode demonstrates superior electrochemical performance to other RMAC electrodes. Moreover, the doping of heteroatoms such as nitrogen/oxygen/phosphorus/sulfur is also beneficial for increasing the electrical conductivity and wettability of the active carbon material, which further improves the ion transfer efficiency and capacity.[67]

Fig. S6 (ESI†) illustrates the electrochemical stability of RMAC-4 by means of a recycling test implemented at 10 A g^{-1}. Apparently, the specific capacitance decreases gradually in pace with the increase of the charge–discharge cycle number. Importantly, the electrode retained 93.6% of its initial specific capacity after 10 000 charge–discharge cycles at a high current density (10 A g^{-1}). The superior electrochemical stability can be ascribed to the preserved structure after long-term

cycling. The relatively stable coulombic efficiency slightly exceeding 100% is also indicated for the RMAC-4 electrode. The phenomenon could illustrate that the enhanced wettability of the carbon surface to the electrolyte solution along with reaction time could contribute to the interfacial area and ion diffusion in the interface between the electrolyte and the electrode material[68] (Fig. 7).

Generally, the excellent performances of RMACs are attributed to the high specific surface area and broadened pore distribution, as well as heteroatom doping, which can not only prevent the formation of long complicated channels, but also provide sufficient storage sites for charges and ions.

3.3 Supercapacitor performance

The CV curves of the supercapacitor (Fig. 8a) maintain a near-rectangular shape at scan rates varying from 2 to 200 mV s^{-1}, revealing a typical electrostatic double layer capacitance (EDLC).[69] According to the graph, the shape of the CV curves still remain unchanged even at a high scan rate (200 mV s^{-1}), confirming excellent stability and capacitive and charge storing properties of the electrodes even in the fast charge-transfer process.[70] The high specific capacitance at lower scan rates is put down to facile diffusion and high movement of the electrolyte ions into the active material. Spontaneously, much more time maybe beneficial for enhanced interaction between the electrolyte ions and the ions of the deposited active carbon material at a lower scan rate. As the scan rate increase to higher values, the reduction in the specific capacitance is ascribed to the deficiency of time for the ions in motion to fill the spaces of active material, and further leads to limited interactions on the outer surfaces only.[71] Therefore, some active parts of the surface areas at higher scan rates may be adverse for charge storage.

According to Nyquist plots for RMAC-4 (Fig. 8b), the semicircles in the high frequency region correspond to the resistance of charge transfer at the electrolyte/electrode interface (R_{ct}), while the oblique straight lines in the low frequency region are bound up with the K$^+$ diffusion process. Based on the Nyquist plot, the series resistance (R_s) of the supercapacitor (2.43 Ω) at 10.2 kHz calculated from the intercept of the high-frequency semicircle on the real axis demonstrates small charge transfer resistance and low Warburg resistance for fast ion diffusion at the electrode/electrolyte interface due to its better compatibility with the aqueous electrolyte.[72]
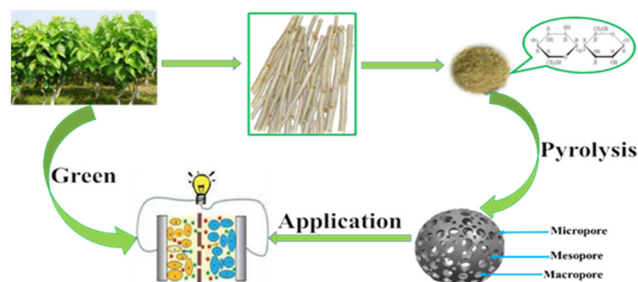

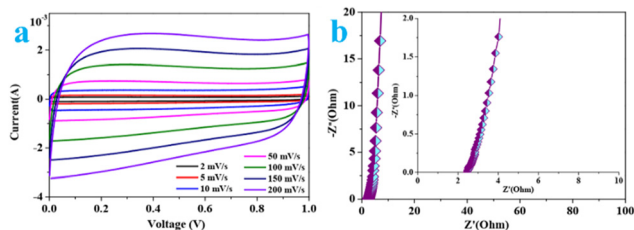**Fig. 7** Schematic illustration of the formation of the supercapacitor.

Fig. 8 (a) CV curves of the RMAC//RMAC symmetrical supercapacitor at different scan rates in the voltage window of 0–1.0 V and (b) Nyquist plots of the RMAC//RMAC symmetrical supercapacitor.

As for the GCD curves shown in Fig. 9a, similar shapes with relatively low voltage drop at various current densities are indicated, confirming a steady rate property of the supercapacitor and a fast ion transfer kinetics in the KOH aqueous electrolyte.[73] The analysis of these findings reveals the typical "triangular galvanostatic profile" predicted for well-behaved SCs. On account of the charge–discharge time along with the current density, the specific capacitance of the RMAC//RMAC decrease from 1 to 20 A g^{-1} due to kinetic limitations (Fig. 9b). The measured specific capacitance values at the current densities of 1–20 A g^{-1} are 296.15, 231.48, 192.45, 153.64 and 106.82 F g^{-1}, respectively. The supercapacitor maintains 51.88% of its initial specific capacitance even at a current density of 10 A g^{-1}, which demonstrates that the high-performance electrode achieves remarkable rate capability. The superior electrochemical property essentially is correlated with the doping of the heteroatoms and the rich defects of the amorphous structure that contribute to the electron/ion transfer.[74]

The excellent areal capacitance and high rate capability confirm superior energy storage performance of the symmetrical RMACs. To validate the applicability of RMAC-4 as a power source (Fig. 10a), the energy and power densities based on the total mass of active materials in the two electrodes are calculated from the GCD profiles. Impressively, RMAC//RMAC achieves an energy density of around ~59.23 W h kg^{-1} at a power density of 1.2 kW kg^{-1}. Moreover, an energy density value of ~21.364 W h kg^{-1} could also be attained at

24 kW kg^{-1}. Such remarkable energy and power densities are superior to commercial supercapacitors (3–5 W h kg^{-1}) and other carbonaceous symmetric supercapacitors derived from biomass[75–77] and comparable to the performance of some asymmetric suppercapacitors.[55,78] The superior functions could be ascribed to the special structure of the carbon materials such as an ultrahigh specific surface area and broadened pore distribution as well as heteroatom doping, which contribute to rapid ion diffusion, ample charge storage, and additional pseudo-capacitance.[79]

In our case, the GCD cycling profiles are obtained to investigate the cycling stability of the supercapacitor at a current load of 10 A g^{-1} (Fig. 10b). After 10 000 cycles, there is a loss of only 8.4% compared with the starting specific capacitance value, revealing the good cycling stability for its potential practical application. A small attenuation for the supercapacitors can be ascribed to the increased electrical resistance in the devices. The outstanding cycling stability may be attributed to the firm bonding of the functional groups to the carbon surface in the process of the cycling, and the reversible Faraday reactions originating from the surface functionalgroups.[80]

In addition, the supercapacitor based on RMAC can be employed in various electronics. According to Fig. S7, (ESI†) the operating voltage range could be further broadened by the linking two or three devices. A tandem device could lighten a red light-emitting-diode lamp (LED, the lowest working potential is 2.0 V). These LEDs can be continuously powered on. These results demonstrate that the symmetric RMACs satisfy the requirements of practical energy storage devices. Moreover, the approach is considerably prospective to switch on the window for legitimately devising ideal hierarchical porous carbon materials as the electrode material, and further contributing to the synthesis guidance of high-energy storage materials for supercapacitors.

Conclusions

In summary, the advantages of eco-friendliness, simplicity, and scalability of the KOH activating method have been exploited to synthesize nanoscale RMAC samples. The plenty of hierarchical
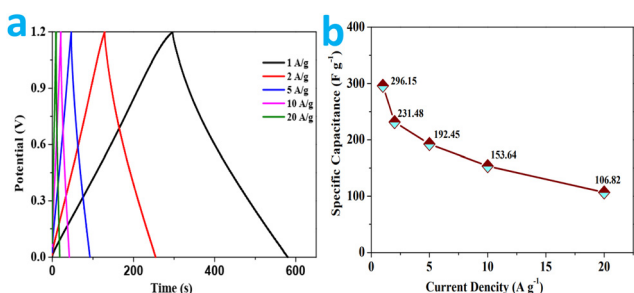

Fig. 9 (a) Galvanostatic charge/discharge curves of the RMAC//RMAC symmetrical supercapacitor at different current densities; (b) specific capacitances of the as-assembled RMAC symmetrical supercapacitor based on the total mass of the active materials of the two electrodes at different current densities.
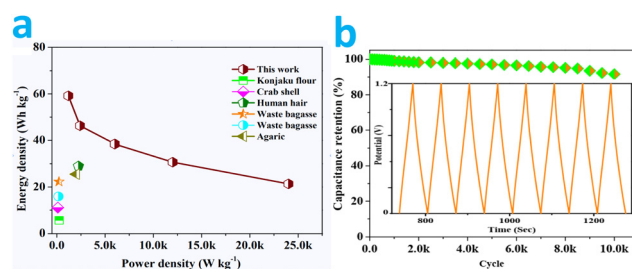

Fig. 10 (a) Ragone plots of the RMAC symmetrical supercapacitor and other previously reported carbon-based symmetrical supercapacitors and (b) cycle performance of the RMAC symmetrical supercapacitor at a current density of 10 A g^{-1} (inset photograph of the GCD electrode curves for recycling).

pores and high specific surface area of the as-synthesized materials contribute to superior electrochemical performances. RMAC-4 presents a capacitance of $\sim$796 F g^{-1} at 1 A g^{-1} and the cycling performances with 93.6% retention after 10 000 cycles. Moreover, the RMAC//RMAC devices demonstrate a good specific capacitance of $\sim$296 F g^{-1} at 1 A g^{-1}, and a superior energy density of $\sim$59 W h kg^{-1} at 1.2 kW kg^{-1} as well as high cycling stability with depletion of 8.4% capacitance after 10 000 cycles. The assembled devices exhibit considerable specific capacitance, operational stability, and synergetic energy–power output characteristics in practical applications, which will improve the industrialization of biomass materials for green and sustainable energy storage devices.

Conflicts of interest

There are no conflicts to declare.

Acknowledgements

References

1 S. G. Krishnan, A. Arulraj, P. Jagadish, M. Khalid, M. Nasrollahzadeh, R. Fen, C. C. Yang and G. Hegde, *Crit. Rev. Solid. State*, 2022, DOI: 10.1080/10408436.2022.2027225.

2 F. El-Kady, V. Strong, S. Dubin and R. Kaner, *Science*, 2012, **335**, 1326.

3 J. Acharya, G. P. Ojha, B. Pant and M. Park, *J. Mater. Chem. A*, 2021, **9**, 23977.

4 J. J. Zhu, Y. Sun, J. Gao, Z. B. Qin, Y. N. Zhou, R. Tian and Y. Gao, *Chem. Commun.*, 2022, **58**, 5861.

5 S. S. Bengtsen, L. Hamelin, L. Bregnbæk, L. Zou and M. Münster, *Energy Environ. Sci.*, 2022, **15**, 1950.

6 D. K. Lee, D. Lee, M. A. Lumley and K.-S. Choi, *Chem. Soc. Rev.*, 2019, **48**, 2126.

7 S. Liu, D. Ni, H. F. Li, K. N. Hui, C. Y. Ouyang and S. C. Jun, *J. Mater. Chem. A*, 2018, **6**, 10674.

8 S. W. Zhang, B. S. Yin, X. X. Liu, D. M. Gu, H. Gong and Z. B. Wang, *Nano Energy*, 2019, **59**, 41.

9 W. Song, X. Teng, Y. Liu, J. Wang, Y. Niu, X. He, C. Zhang and Z. Chen, *Nanoscale*, 2019, **11**, 6401.

10 C. Miao, C. Zhou, H. E. Wang, K. Zhu, K. Ye, Q. Wang, J. Yan, D. Cao, N. Li and G. Wang, *J. Power Sources*, 2021, **490**, 229532.

11 J. Acharya, G. P. Ojha, B. S. Kim, B. Pant and M. Park, *ACS Appl. Mater. Interfaces*, 2021, **13**, 17487.

12 X. T. Ren, N. Meng, L. Ventura, S. Goutianos, E. Barbieri, H. Zhang, H. X. Yan, M. J. Reece and E. Bilotti, *J. Mater. Chem. A*, 2022, **10**, 10171.

13 M. Kumar and T. C. Nagaiah, *J. Mater. Chem. A*, 2022, **10**, 10979.

14 Z. H. Huang, Y. Song, D. Y. Feng, Z. Sun, X. Sun and X. X. Liu, *ACS Nano*, 2018, **12**, 3557.

15 S. Q. Zhu, J. C. Shu and M. S. Cao, *Nanoscale*, 2022, **14**, 7322.

16 R. T. Zhou, Y. Li and K. H. Lam, *J. Mater. Chem. A*, 2021, **9**, 21302.

17 J. H. Lee, S. P. Park, K. Park and H. J. Kim, *Adv. Funct. Mater.*, 2020, **30**, 1907437.

18 C. C. Zhang, Q. Li, T. D. Wang, Y. D. Miao, J. Q. Qi, Y. W. Sui, Q. K. Meng, F. X. Wei, L. Zhu, W. Zhang and P. Cao, *Nanoscale*, 2022, **14**, 6339.

19 X. Zhao, P. Pachfule and A. Thomas, *Chem. Soc. Rev.*, 2021, **50**, 6871.

20 P. B. Geng, S. S. Zheng, H. Tang, R. M. Zhu, L. Zhang, S. Cao, H. G. Xue and H. Pang, *Adv. Energy Mater.*, 2018, **8**, 1703259.

21 D. W. Wang, J. W. Nai, H. Li, L. Xu and Y. T. Wang, *Carbon*, 2019, **141**, 40.

22 D. W. Wang, J. W. Nai, L. Xu and T. Sun, *ACS Sustainable Chem. Eng.*, 2019, **7**, 18901.

23 P. C. Zhou, F. Xiao, R. X. Weng, Q. G. Huang, L. Wang, Q. H. He, W. S. Tang, P. L. Yang, R. Su, P. He, B. Jia and L. Bian, *J. Mater. Chem. A*, 2022, **10**, 10514.

24 Z. Li, J. J. Wei, J. Ren, X. M. Wu, L. Wang, D. Y. Pan and M. H. Wu, *Carbon*, 2019, **154**, 410.

25 Z. Q. Li, Y. Yang, G. H. Ding, L. Z. Wei, G. Yao, H. L. Niu, F. C. Zheng and Q. W. Chen, *J. Mater. Chem. A*, 2022, **10**, 10033.

26 R. W. Shu, Z. L. Wan, J. B. Zhang, Y. Wu, Y. Liu, J. J. Shi and M. D. Zheng, *ACS Appl. Mater. Interfaces*, 2020, **12**, 4689.

27 S. F. Chen, C. J. Zhu, W. P. Xian, X. Y. Liu, X. L. Liu, Q. H. Zhang, S. Q. Ma and Q. Sun, *J. Am. Chem. Soc.*, 2021, **143**(25), 9415.

28 D. Y. Gao, Y. F. Pan, J. H. Wei, D. D. Han, P. C. Xu, Y. Wei, L. C. Mao and X. H. Yin, *J. Mater. Chem. A*, 2022, **10**, 11186.

29 X. Liu, W. Q. Yuan and R. Y. Zhao, *ACS Food Sci. Technol.*, 2021, **1**(6), 1041.

30 S. Zhang, P. C. Dai, H. J. Liu, L. T. Yan, H. X. Song, D. D. Liu and X. B. Zhao, *ACS Appl. Energy Mater.*, 2020, **3**(12), 12627.

31 I. Mukherjee, V. Cilamkoti and R. K. Dutta, *ACS Appl. Nano Mater.*, 2021, **4**(8), 7686.

32 S. Zhi, X. Tang, Z. N. Zheng, F. X. Xu, Y. H. Ren and X. L. Wang, *Russ. J. Plant Physiol.*, 2020, **67**(4), 703.

33 Z. Y. Liu, Y. Yang, Y. N. Yuan, L. D. Wang, J. Sheng and W. D. Fei, *J. Mater. Chem. A*, 2022, **10**, 10427.

34 Z. Xu, F. Xie, J. Wang, H. Au, M. Tebyetekerwa, Z. Y. Guo, S. Y. Yang, Y. S. Hu and M. M. Titirici, *Adv. Funct. Mater.*, 2019, **29**, 1903895.

35 H. Peng, B. Yao, X. Wei, T. Liu, T. Kou, P. Xiao, Y. Zhang and Y. Li, *Adv. Energy Mater.*, 2019, **9**, 1803665.

36 Y. Q. Shan, Z. X. Xu, P. G. Duan, H. L. Fan, X. Hu and R. Luque, *ACS Sustainable Chem. Eng.*, 2020, **8**, 15809.

37 K. Jayaramulu, M. Horn, A. Schneemann, H. Saini, A. Bakandritsos, V. Ranc, M. Petr, V. Stavila, C. Narayana,

B. Scheibe, Š. Kment, M. Otyepka, N. Motta, D. Dubal, R. Zbořil and R. A. Fischer, *Adv. Mater.*, 2021, **33**, 2004560.

38 L. M. Chen, H. Y. Yu, Z. H. Li, X. Chen and W. L. Zhou, *Nanoscale*, 2021, **13**, 17837.

39 K. Zhang, H. Y. Zeng, M. X. Wang, H. B. Li, W. Yan, H. B. Wang and Z. H. Tang, *J. Mater. Chem. A*, 2022, **10**, 11213.

40 C. Dang, Z. Huang, Y. Chen, S. Zhou, X. Feng, G. Chen, F. Dai and H. Qi, *ACS Appl. Mater. Interfaces*, 2020, **12**, 21528.

41 C. X. Guo and C. M. Li, *Energy Environ. Sci.*, 2011, **4**, 4504.

42 Z. Bi, Q. Kong, Y. Cao, G. Sun, F. Su, X. Wei, X. Li, A. Ahmad, L. Xie and C. M. Chen, *J. Mater. Chem. A*, 2019, **7**, 16028.

43 Y. Dong, S. Zhang, X. Du, S. Hong, S. Zhao, Y. Chen, X. Chen and H. Song, *Adv. Funct. Mater.*, 2019, **29**, 1901127.

44 T. X. Ma, Y. Z. Pan, J. Y. Chen, Z. M. Yan, B. X. Chen, L. Zhao, L. W. Hu, L. Y. Wen and M. L. Hu, *J. Mater. Chem. A*, 2022, **10**, 9932.

45 J. L. W. Morgan, J. Strumillo and J. Zimmer, *Nature*, 2013, **493**, 181.

46 S. Y. Wang, Z. W. Hu, Z. M. Pan and D. W. Wang, *J. Alloys Compd.*, 2021, **876**, 160203.

47 T. Shang, Y. Xu, P. Li, J. Han, Z. Wu, Y. Tao and Q. H. Yang, *Nano Energy*, 2020, **70**, 104531.

48 C. Li, Y. W. Ding, B. C. Hu, Z. Y. Wu, H. L. Gao, H. W. Liang, J. F. Chen and S. H. Yu, *Adv. Mater.*, 2020, **32**, 1904331.

49 C. Liu, H. Wang, X. Zhao, H. Liu, Y. Sun, L. Tao, M. Huang, J. Shi and Z. Shi, *J. Power Sources*, 2020, **457**, 228056.

50 R. Guo, C. Lv, W. Xu, J. Sun, Y. Zhu, X. Yang, J. Li, J. Sun, L. Zhang and D. Yang, *Adv. Energy Mater.*, 2020, **10**, 1903652.

51 Z. X. Xu, X. Q. Deng, S. Zhang, Y. F. Shen, Y. Q. Shan, Z. M. Zhang, R. Luque, R. Luque, P. G. Duan and X. Hu, *Green Chem.*, 2020, **22**, 3885.

52 Y. Yang, K. P. Wang, Q. Zang, Q. Q. Shi, Y. W. Wang, Z. Y. Xiao, Q. Zhang and L. Wang, *J. Mater. Chem. A*, 2022, **10**, 11277.

53 H. Luo, P. Xiong, J. Xie, Z. Yang, Y. Huang, J. Hu, Y. Wan and Y. Xu, *Adv. Funct. Mater.*, 2018, **28**, 1803075.

54 S. Qiu, L. Xiao, M. L. Sushko, K. S. Han, Y. Shao, M. Yan, X. Liang, L. Mai, J. Feng, Y. Cao, X. Ai, H. Yang and J. Liu, *Adv. Energy Mater.*, 2017, **7**, 1700403.

55 D. W. Wang, S. Y. Wang and Z. M. Lu, *Int. J. Energy Res.*, 2021, **2**, 2498.

56 X. Yang, Q. Wang, K. Zhu, K. Ye, G. Wang, D. Cao and J. Yan, *Adv. Funct. Mater.*, 2021, **31**, 2101087.

57 X. Tang, H. Zhou, Z. Cai, D. Cheng, P. He, P. Xie, D. Zhang and T. Fan, *ACS Nano*, 2018, **12**, 3502.

58 L. Zhang, C. Yang, N. Hu, Z. Yang, H. Wei, C. Chen, L. Wei, Z. J. Xu and Y. Zhang, *Nano Energy*, 2016, **26**, 668.

59 X. Li, H. Li, X. Fan, X. Shi and J. Liang, *Adv. Energy Mater.*, 2020, **10**, 1903794.

60 X. Wang, H. Li, H. Li, S. Lin, W. Ding, X. Zhu, Z. Sheng, H. Wang, X. Zhu and Y. Sun, *Adv. Funct. Mater.*, 2020, **30**, 1910302.

61 J. Yan, Q. Wang, T. Wei and Z. Fan, *Adv. Energy Mater.*, 2014, **4**, 1300816.

62 M. Lv, X. Zhang, F. Wang, T. Yu, H. Lv, Y. Zhai, Y. Shen and G. Lv, *Nanotechnology*, 2020, **31**, 225603.

63 X. Y. Zhao, Q. Bi, C. Yang, K. Tao and L. Han, *Dalton Trans.*, 2021, **50**, 15260.

64 F. Wang, X. Wu, X. Yuan, Z. Liu, Y. Zhang, L. Fu, Y. Zhu, Q. Zhou, Y. Wu and W. Huang, *Chem. Soc. Rev.*, 2017, **46**, 6816.

65 W. Raza, F. Ali, N. Raza, Y. Luo, K.-H. Kim, J. Yang, S. Kumar, A. Mehmood and E. E. Kwon, *Nano Energy*, 2018, **52**, 441.

66 B. Dunn, H. Kamath and J. M. Tarascon, *Science*, 2011, **334**, 928.

67 Y. Wang and Y. Xia, *Adv. Mater.*, 2013, **25**, 5336.

68 A. Bavykina, N. Kolobov, I. S. Khan, J. A. Bau, A. Ramirez and J. Gascon, *Chem. Rev.*, 2020, **120**, 8468.

69 P. Zhang, B. Y. Guan, L. Yu and X. W. Lou, *Angew. Chem., Int. Ed.*, 2017, **56**, 7141.

70 Y. Zhang, N. Cao, S. Szunerits, A. Addad, P. Roussel and R. Boukherroub, *Chem. Eng. J.*, 2019, **374**, 347.

71 M. K. Peng, W. Z. Yang, L. B. Li, K. Y. Zhang, L. Wang, T. Hu, K. Yuan and Y. W. Chen, *Chem. Commun.*, 2021, **57**, 10731.

72 X. Gao, X. Du, T. S. Mathis, M. Zhang, X. Wang, J. Shui, Y. Gogotsi and M. Xu, *Nat. Commun.*, 2020, **11**, 6160.

73 X. F. Chen, Y. Z. Zhu, M. Zhang, J. Y. Sui, W. C. Peng, Y. Li, G. L. Zhang, F. B. Zhang and X. B. Fan, *ACS Nano*, 2019, **13**, 9449.

74 Y. Cao, X. Tian, J. Gu, B. Liu, B. Zhang, S. Song, F. Fan and Y. Chen, *Angew. Chem., Int. Ed.*, 2018, **57**, 4543.

75 Y. Zhang, S. Liu, X. Zheng, X. Wang, Y. Xu, H. Tang, F. Kang, Q. H. Yang and J. Luo, *Adv. Funct. Mater.*, 2017, **27**, 1604687.

76 M. Zohair, K. Moyer, J. E. Rathert, C. Meng, J. Waugh and C. L. Pint, *ACS Nano*, 2020, **14**, 2308.

77 B. Zhu, B. Liu, C. Qu, H. Zhang, W. Guo, Z. Liang, F. Chen and R. Zou, *J. Mater. Chem. A*, 2018, **6**, 1523.

78 D. W. Wang, Z. M. Pan, G. X. Chen and Z. M. Lu, *Electrochim. Acta*, 2021, **379**, 138170.

79 Y. Shabangoli, M. S. Rahmanifar, M. F. El-Kady, A. Noori, M. F. Mousavi and R. B. Kaner, *Adv. Energy Mater.*, 2018, **8**, 1802869.

80 W. Yan, J. Su, Z. M. Yang, S. Lv, Z. Jin and J. L. Zuo, *Small*, 2021, **17**, 200520.